


Magnetic proximity enabled bulk photovoltaic effects in van der Waals heterostructures

Xingchi Mu, Qianqian Xue, Yan Sun, and Jian Zhou*

Center for Alloy Innovation and Design, State Key Laboratory for Mechanical Behavior of Materials, Xi'an Jiaotong University, Xi'an 710049, China

 (Received 17 August 2022; revised 9 November 2022; accepted 19 December 2022; published 3 January 2023)

The bulk photovoltaic (BPV) effect, a second-order nonlinear process that generates static current under light irradiation, requires centrosymmetric broken systems as its application platform. To realize measurable BPV photocurrent in spatially centrosymmetric materials, various schemes such as chemical doping, structural deformation, or electric bias have been developed. In this paper, we suggest that the magnetic proximity effect via van der Waals (vdW) interfacial interaction, a contact-free strategy, also breaks the centrosymmetry and generates large BPV currents. Using the Bi_2Te_3 quintuple layer as an exemplary material, we show that magnetic proximity effect from MnBi_2Te_4 septuple layers yields a finite and tunable shift and injection photocurrents. We apply group theory and first-principles calculations to evaluate the layer-specific shift and injection current generations under linearly polarized light irradiation. We find that the magnetic injection photoconductivity that localized on the Bi_2Te_3 layer can reach $>70 \times 10^8 \text{ A}/(\text{V}^2 \text{ s})$, so that a one-dimensional linear current density on the order of 0.1 mA/nm can be achieved under an intermediate intensity light. In addition to charge current, we also extend our discussions into spin BPV current, giving pure photogenerated spin current. The vertical propagation direction between the charge and spin photocurrents suggests that they can be used individually in a single material. Compared with previously reported methods, the magnetic proximity effect via vdW interface does not significantly alter the intrinsic feature of the centrosymmetric material (e.g., Bi_2Te_3), and its manipulation can be easily achieved by the proximate magnetic configurations (of MnBi_2Te_4), interlayer distance, and light polarization.

DOI: [10.1103/PhysRevResearch.5.013001](https://doi.org/10.1103/PhysRevResearch.5.013001)

I. INTRODUCTION

The bulk photovoltaic (BPV) effect [1–3] that converts light irradiation into electric current in a single material, which could avoid the traditional $p-n$ semiconductor heterojunction fabrications [4,5], has been attracting tremendous interest recently. In centrosymmetric (\mathcal{P}) broken systems, light induces anharmonic motion of carriers (electrons in the conduction bands and holes in the valence bands). Hence, two typical second-order nonlinear optical processes, namely, sum frequency and difference frequency generations, occur simultaneously [6,7]. The BPV effect arises from the difference frequency generation process under monochromatic irradiation (with angular frequency of ω). Two major mechanisms of BPV processes that have been extensively studied are shift current and injection current generations, both of which originate from the geometric phases of electronic states (such as the Berry phase) that strongly rely on symmetry constraints [8–10]. Under time-reversal symmetry \mathcal{T} , shift current

emerges through linearly polarized light (LPL) illumination:

$$j_{\text{NSC}}^a = \sigma_{\text{NSC}}^{a,bc}(0, \omega, -\omega) E^b(\omega) E^c(-\omega), \quad (1)$$

where j_{NSC}^a indicates normal shift current (NSC) density that is induced by light-alternating electric field $\mathbf{E}(\omega)$. Here, $\sigma_{\text{NSC}}^{a,bc}(0, \omega, -\omega)$ is the NSC photoconductivity coefficient, with a , b , and c referring to Cartesian axes. The $\sigma_{\text{NSC}}^{a,bc}(0, \omega, -\omega)$ scales with the shift vector between the valence and conduction bands. On the other hand, the circularly polarized light (CPL) produces normal injection current (NIC):

$$\frac{dj_{\text{NIC}}^a}{dt} = \eta_{\text{NIC}}^{a,bc}(0, \omega, -\omega) E^b(\omega) E^c(-\omega). \quad (2)$$

The injection current density grows with time t and saturates at the carrier relaxation time τ . Therefore, one usually discusses the photoconductivity $\eta_{\text{NIC}}^{a,bc}(0, \omega, -\omega)$ for the time derivative of current density j_{NIC}^a . The NIC photoconductivity scales with interband Berry curvature. Hence, both shift and injection currents arise from the quantum topological nature of electronic wave functions.

Very recently, it has been disclosed that, for magnetic \mathcal{T} -broken systems, there are two additional cousin photocurrent mechanisms, namely, magnetic shift current (MSC) and magnetic injection current (MIC). For example, Wang and Qian [11] have shown that these magnetic version photocurrents emerge in antiferromagnetic (AFM) MnBi_2Te_4 bilayers with \mathcal{PT} -symmetry. Similar BPV currents have also been

*jjanzhou@xjtu.edu.cn

Published by the American Physical Society under the terms of the [Creative Commons Attribution 4.0 International license](https://creativecommons.org/licenses/by/4.0/). Further distribution of this work must maintain attribution to the author(s) and the published article's title, journal citation, and DOI.

evaluated in the AFM CrI₃ bilayers [12,13], and their fundamental mechanisms have been revealed [14]. In these cases, the symmetry arguments and numerical calculations demonstrate that both NSC and NIC would vanish. For the \mathcal{PT} systems, the LPL and CPL irradiation could induce MIC and MSC, respectively. Depending on specific materials, their existence can be determined by group theory (see Refs. [11–14] and the Supplemental Material [15] for detailed discussions).

To conceive finite photocurrents, as stated previously, one must resort to \mathcal{P} -broken systems. This excludes many spatially centrosymmetric materials, unless they are chemically doped (or alloyed) [16], structurally deformed [17–20], or electrically biased [21,22]. These schemes could effectively break \mathcal{P} in either transient or permanent strategies but usually require direct contacts with the samples in chemical, electrochemical, and/or mechanical techniques. In this paper, we propose that magnetic proximity effect [23] is another facile and controllable method to manipulate the centrosymmetry in van der Waals (vdW) layers and generate large layer-resolved BPV currents. Note that the vdW interactions are sufficiently weak (on the order of 1–10 $\mu\text{J}/\text{cm}^2$) [24,25] and are less susceptible to lattice distortions or crystal damages. The magnetic proximity effect through the vdW gap is even marginal (on the order of 0.1 $\mu\text{J}/\text{cm}^2$). We use MnBi₂Te₄ (denoted as MBT) bilayer and Bi₂Te₃ (denoted as BT) to build superlattice thin films to illustrate our theory and apply first-principles calculations to evaluate their layer-resolved BPV currents. These superlattices possess the same magnetic point group with bilayer MBT [$\bar{3}'m'$ for an interlayer AFM and $\bar{3}m'$ for an interlayer ferromagnet (FM)]. They have been recently fabricated and host versatile intrinsic magnetic topological features, such as the quantum anomalous Hall effect and the axion insulating phase [26–31]. The MBT septuple layer (SL) comprises seven atomic layers (Te-Bi-Te-Mn-Te-Bi-Te), which are vdW separated by BT quintuple layers (QLs, Te-Bi-Te-Bi-Te) with small interlayer binding energy of 52 $\mu\text{J}/\text{cm}^2$ (comparable with other transition metal chalcogenides and halides) [32,33]. The Mn 3*d* magnetic moments favor a long-range interlayer AFM coupling and a normal intralayer FM magnetic configuration below its Néel temperature (~ 20 K depending on superlattice structures) [34]. This breaks \mathcal{T} while preserving \mathcal{PT} in the whole system. Even though the BT QLs are crystalline centrosymmetric and intrinsically nonmagnetic, we perform first-principles density functional theory (DFT) calculations and show that sizable and large BPV currents emerge in the BT QL. This is due to the magnetic proximity effect that arises from MBT SLs through the vdW gap, so that \mathcal{P} is broken in the magnetic point group framework. To be specific, we calculate the NSC and MIC projected onto different vdW layers. At the AFM ground state, a finite photocurrent emerges in the BT QLs, and its MIC photoconductivity can be as large as $72.4 \times 10^8 \text{ A}/(\text{V}^2 \text{ s})$. The photocurrent density increases with the quadratic power of electric field (or linear relation with light intensity). For example, under a LPL with intensity of $3.3 \times 10^{10} \text{ W}/\text{cm}^2$ (electric field magnitude of 0.5 V/nm), the photocurrent density reaches $361.8 \mu\text{A}/\text{nm}^2$, assuming a conservative carrier lifetime of 0.2 ps. We also show that the magnetic configuration of MBT SLs controls the magnitude and direction of different photocurrents. The calculations reveal that time

reversal of the AFM pattern would reverse the MIC while keeping the NSC, as the former is \mathcal{T} odd and the latter is \mathcal{T} even. If the interlayer magnetic configurations between MBT SLs are driven to be FM, \mathcal{P} preserves rather than \mathcal{PT} . The layer-resolved photocurrents in the BT QLs then vanish completely. The *z*-magnetic moment confines the system with \mathcal{C}_{3z} ; hence, a different LPL polarization direction changes the BPV current as well. We also extend our calculations and discuss the BPV spin current. The spin current has a surplus spin S_z that transforms as a pseudovector. Under LPL irradiation, it also composes MIC and NSC nature. The former is \mathcal{T} even, while the latter is \mathcal{T} odd. Therefore, the spin current, in the same manner, can be fine-tuned via both magnetic alignments and light polarization.

II. METHODS

A. DFT

The first-principles calculations are implemented in the Vienna *Ab initio* Simulation Package [35,36] which adopts the projector augmented-wave method [37] and the plane-wave basis set (cutoff energy of 350 eV) to treat the core and valence electrons, respectively. The exchange-correlation functional treatment uses the generalized gradient approximation in the solid state Perdew-Burke-Ernzerhof form [38]. The periodic boundary condition is used, and the first Brillouin zone (BZ) is represented by a Γ -centered \mathbf{k} -mesh with $15 \times 15 \times 1$ grid [39]. To incorporate the strong correlations on magnetic Mn 3*d* orbitals, we add an effective Hubbard U ($= 5.34 \text{ eV}$) correction according to the Dudarev scheme [40,41]. This value has been widely used in previous works and has been demonstrated to yield results consistent with experimental observations [42–44]. One notes that other U values could give qualitatively same results. A vacuum space of at least 15 Å is added in the out-of-plane *z* direction to eliminate the artificial interaction between different images under the periodic boundary condition. Self-consistent spin-orbit coupling (SOC) interactions have been used in all calculations. The convergence criteria for total energy and the force component are set to be $1 \times 10^{-7} \text{ eV}$ and $0.01 \text{ eV}/\text{Å}$, respectively. The vdW interactions are semi-empirically included in the zero damping DFT-D3 method [45].

B. BPV conductivities

The BPV photoconductivity coefficients are calculated using the Wannier representation, which includes Mn *d*, Bi *p*, and Te *p* (covering all bands from -6.2 to 4.8 eV relative to the Fermi level) to fit the DFT electronic structures [46–48]. A dense \mathbf{k} -mesh grid of $601 \times 601 \times 1$ is adopted to integrate the first BZ to obtain the optical conductivities, which has been tested to achieve sufficient converged accuracy. According to the quadratic order Kubo perturbation theory, the BPV photoconductivity can be evaluated in various gauge schemes. The velocity gauge approach, which tends to diverge at low incident frequency, can be simplified into different photocurrents at the long carrier lifetime limit [49–52]. In detail, one

can apply band theory to evaluate the NSC and MIC conductance coefficients separately:

$$\sigma_{\text{NSC}}^{a,bc}(0, \omega, -\omega) = \frac{\pi e^3}{2\hbar^2} \int \frac{d^3\mathbf{k}}{(2\pi)^3} \sum_{n,m} f_{nm} \text{Im}(r_{mn}^b r_{nm}^{c;a} + r_{mn}^c r_{nm}^{b;a}) \times \delta(\omega_{nm} - \omega), \quad (3)$$

and

$$\eta_{\text{MIC}}^{a,bc}(0, \omega, -\omega) = -\frac{\pi e^3}{2\hbar^2} \int \frac{d^3\mathbf{k}}{(2\pi)^3} \sum_{n,m} f_{nm} \Delta_{nm}^a \times (r_{mn}^b r_{nm}^c + r_{mn}^c r_{nm}^b) \delta(\omega_{mn} - \omega), \quad (4)$$

Here, the position operator matrix is defined as $r_{nm}^a = \frac{v_{nm}^a}{i\omega_{nm}} = \frac{\langle n | \frac{\partial H}{\partial k^a} | m \rangle}{i\omega_{nm}}$ ($n \neq m$) with $\omega_{nm} = \omega_n - \omega_m$ measuring the band energy difference between band n and m . Also, $f_{nm} = f_n - f_m$ and $\Delta_{nm}^a = v_{nm}^a - v_{mn}^a$ are occupation and velocity difference, respectively. All quantities depend on reciprocal space coordinate \mathbf{k} , and such \mathbf{k} dependence is omitted in these equations for clarity reason. The Dirac delta function is represented by the Lorentz function with a broadening factor of 0.02 eV, which guarantees the energy conservation law. To analyze the integrand of NSC and MIC, we denote them as $\zeta(\mathbf{k}, \omega) = \sum_{n,m} f_{nm} \text{Im}(r_{mn}^b r_{nm}^{c;a} + r_{mn}^c r_{nm}^{b;a}) \delta(\omega_{nm} - \omega)$ and $\zeta(\mathbf{k}, \omega) = \sum_{n,m} f_{nm} \Delta_{nm}^a (r_{mn}^b r_{nm}^c + r_{mn}^c r_{nm}^b) \delta(\omega_{mn} - \omega)$, respectively. The sum rule for derivative of \mathbf{r} is

$$\begin{aligned} r_{nm}^{b;a} &= \frac{\partial r_{nm}^b}{\partial k^a} - i(A_{nn}^a - A_{mm}^a) r_{nm}^b \\ &= \frac{i}{\omega_{nm}} \left[\frac{v_{nm}^b \Delta_{nm}^a + v_{nm}^a \Delta_{nm}^b}{\omega_{nm}} - w_{nm}^{ba} \right. \\ &\quad \left. + \sum_{l \neq n,m} \left(\frac{v_{nl}^b v_{lm}^a}{\omega_{lm}} - \frac{v_{nl}^a v_{lm}^b}{\omega_{nl}} \right) \right], \end{aligned} \quad (5)$$

where $w_{nm}^{ba} = \langle n | \frac{\partial^2 H}{\partial k^b \partial k^a} | m \rangle$. Both $\sigma_{\text{NSC}}^{a,bc}(0, \omega, -\omega)$ and $\eta_{\text{MIC}}^{a,bc}(0, \omega, -\omega)$ feature electronic topological characters. One defines the shift vector under LPL irradiation between two bands as

$$\mathbf{R}_{nm}^{a,b} = \frac{\partial \phi_{nm}^b}{\partial k^a} + \mathcal{A}_{nn}^a - \mathcal{A}_{mm}^a, \quad (6)$$

where ϕ_{nm}^b is the complex phase of r_{nm}^b ($= |r_{nm}^b| e^{-i\phi_{nm}^b}$). Therefore, it can be shown that $\mathbf{R}_{nm}^{a,b} |r_{nm}^b|^2 = \text{Im}(r_{mn}^b r_{nm}^{b;a})$, which transforms as a polar vector. On the other hand, the quantum metric tensor is defined as

$$\mathbf{g}_{nm}^{bc} = \{r_{mn}^b, r_{nm}^c\} = (r_{mn}^b r_{nm}^c + r_{mn}^c r_{nm}^b), \quad (7)$$

which demonstrates the topological feature of MIC. Note that, for \mathcal{T} -symmetric systems, the MIC vanishes (under LPL), while the NSC is symmetrically forbidden in \mathcal{PT} systems.

As for spin photocurrent, we adopt the general definition of $\hat{\mathfrak{T}}^{a,d} = \frac{\{\hat{S}_d, \hat{v}^a\}}{2} = \frac{1}{2}(\hat{S}_d \hat{v}^a + \hat{v}^a \hat{S}_d)$, where \hat{S}_d is the spin operator (d is taken to be z in this paper, being the spin-polarization direction). Hence, to evaluate the spin current, we replace the

velocity operator \hat{v}^a by $\hat{\mathfrak{T}}^{a,d}$. For example, the spin-velocity derivative can be written as [53]

$$d_{nm}^{b;a} = \frac{1}{2} \langle n | \{S_d, w^{ab}\} | m \rangle + \sum_{p \neq n} \frac{\mathfrak{T}_{np}^{a,d} v_{pm}^b}{\omega_{np}} + \sum_{p \neq m} \frac{v_{np}^b \mathfrak{T}_{pm}^{a,d}}{\omega_{mp}}. \quad (8)$$

It would reduce to the charge current formula when one takes the spin operator S_d into an identity matrix. Since the MIC only incorporates the intraband contribution of spin current, we can include the spin-torque effect [19]. This is consistent with the proper definition of spin current via $\hat{\mathfrak{T}}^{a,d} = \frac{d(\hat{S}_d r^a)}{dt}$ [54]. In this case, the Onsager relation is maintained, so that the spin current obeys the conservation law of the equation of motion.

To evaluate the layer-resolved current, we introduce a layer projector operator $\hat{P}_L = \sum_{i \in L} |\phi_i\rangle \langle \phi_i|$ with Wannier function $|\phi_i\rangle$ localized on a specific QL or SL [55]. Then we multiply this \hat{P}_L with velocity (or spin current) operator \hat{v}^a (or $\hat{\mathfrak{T}}^{a,d}$), through which one could map the photocurrent onto each vdW layer. We have checked that the summation of each layer-resolved current on all layers is almost the same as the total photocurrent. Hence, the interlayer photocurrent is marginal, as the vdW gap is ~ 3 Å. Note that, in Eqs. (3) and (4), all \mathbf{k} -space integrals are taken in the three-dimensional BZ, and the vacuum contributions have been included. We thus rescale these in-plane photoconductivity coefficients $\sigma_{\text{NSC}}^{a,bc}(0, \omega, -\omega)$ and $\eta_{\text{MIC}}^{a,bc}(0, \omega, -\omega)$ by multiplying a factor $\frac{L_z}{d_{\text{eff}}}$, where L_z is the simulation supercell lattice constant along z and d_{eff} is an effective thickness of the vdW layer [56,57]. In this paper, we use d_{eff} for MBT SL and BT QL of 14 and 11 Å, respectively, which are taken from the thickness values when they form vdW bulk structures.

III. RESULTS

A. Photocurrents of MBT-MBT bilayer ($\text{Mn}_2\text{Bi}_4\text{Te}_8$)

We examine the atomic geometries, electronic behaviors, and magnetic configurations of different MBT and BT superlattice slabs. To maintain the completeness of our study, we first explore the MBT bilayer (MBT-MBT) without BT intercalation [Fig. 1(a)]. The Te atoms serve as termination layers between the MBT, leaving a vdW gap of 2.9 Å. Each Mn carries $\sim 5 \mu_B$ (Bohr magneton) magnetic moments pointing along the easy axis z , and the intralayer coupling is strongly locked to be FM. The interlayer MBT magnetic coupling prefers an AFM configuration. This is usually referred to as the A-type AFM state. We reveal that the magnetic interlayer exchange energy $\Delta E = E_{\text{FM}} - E_{\text{AFM}}$ (E refers to total energy) is 0.43 meV per unit cell ($0.04 \mu\text{J}/\text{cm}^2$). According to previous experimental facts, this AFM ground state can be converted into FM via applying an external magnetic field below its Néel temperature (~ 12 T at 4.5 K or 6 T at 1.6 K) [58].

Figure 1(b) depicts the calculated electronic band dispersion along the high-symmetric \mathbf{k} -path, in the AFM state. One sees a semiconducting feature with a direct bandgap of 88 meV, where both valence band maximum and conduction band minimum locate at the Γ point. The band structure without SOC effect is shown in Fig. S1 in the Supplemental

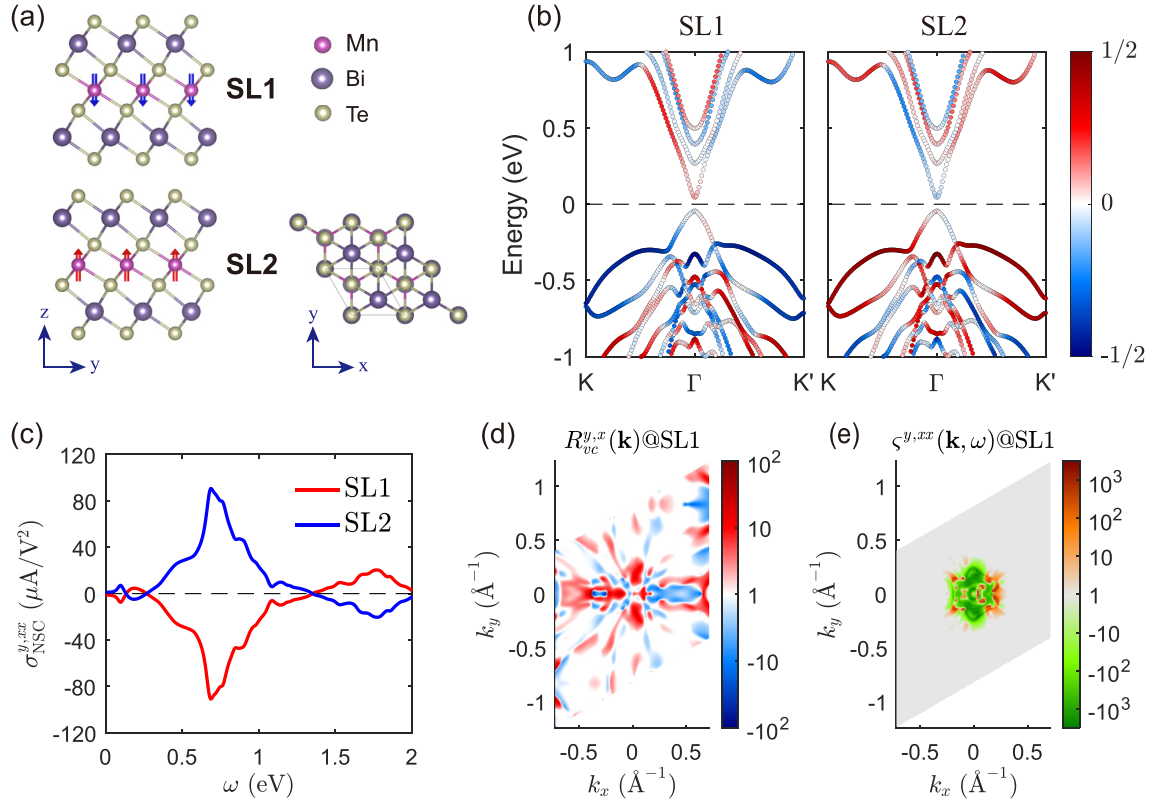


FIG. 1. Structure and normal shift current (NSC) of the MBT-MBT bilayer. (a) Atomic geometric structure of a MBT-MBT bilayer, with arrows in the central Mn atoms representing antiferromagnetic (AFM) moments. Septuple layers (SL1 and SL2) are denoted. Both side view and top view structures are shown. (b) Band dispersion along the high-symmetry \mathbf{k} -path, where different colors represent spin polarization projected onto the two SLs; the spin-orbit coupling effect is considered. (c) The calculated NSC on different MBT SLs under x -linearly polarized light (LPL). The abscissa axis denotes the incident photon frequency ($\hbar = 1$). Only NSC flowing along y is allowed, while the x current is symmetrically forbidden (not shown). (d) Shift vector $R_{vc}^{y,x}(\mathbf{k})$ @SL1 distribution over the first Brillouin zone (BZ) between the top valence (v) and bottom conduction (c) bands. (e) \mathbf{k} -resolved NSC integrand $\zeta^{y,xx}(\mathbf{k}, \omega)$ @SL1 at the incident energy of $\omega = 0.69$ eV, where NSC presents a peak.

Material [15], which gives a larger direct bandgap. This is consistent with the results in previous works [59]. In the AFM configuration (antiunitary \mathcal{PT}), each electronic band state is doubly degenerate without net spin polarization. The layer-dependent spin polarization exhibits a hidden feature. In our results, we use the color scheme to illustrate spin polarizations $\langle S_{nk}^z \rangle$ locally contributed from the SL1 and SL2, which shows opposite values in the two vdW SLs, confirming its hidden spin-polarization character. Note that, in our calculations, we have summed the doubly degenerated state contributions for each n at \mathbf{k} .

We next focus on the NSC and MIC photoconductivities. As discussed previously [60], symmetry operators pose constraints on both photocurrent direction and magnitude. In the whole MBT-MBT bilayer system, the $\bar{3}m'$ symmetry gives only one independent MIC component (symmetrically allowed) [15]. However, when we perform such an analysis on the two MBT SLs individually, their local symmetry reduces and more BPV components will be allowed. In detail, the coordinates of each MBT SL contain a mirror reflection that is normal to the x direction \mathcal{M}_x [Fig. 1(a)]. Since Mn is magnetic along z , one has to multiply an additional time-reversal operator, which gives $\mathcal{M}_x\mathcal{T}$. Thus, the local

group on one MBT SL is reduced to $3m'$, breaking the \mathcal{PT} symmetry. It then yields sizable NSC generation with one independent component (see the Supplemental Material [15]). In detail, the $\mathcal{M}_x\mathcal{T}$ maps BZ coordinate (k_x, k_y) to $(k_x, -k_y)$, which also constrains the shift vector via $\mathcal{M}_x\mathcal{T}R_{nm}^{x,b}(k_x, k_y) = -R_{nm}^{x,b}(k_x, -k_y)$, where $b = x, y$. For example, under x -LPL (or y -LPL) irradiation, the NSC is symmetrically forbidden along x , leaving $\sigma_{\text{NSC}}^{y,xx}(0, \omega, -\omega) \neq 0$. Therefore, we will have layer-resolved NSC generation according to

$$\begin{aligned} J_{\text{NSC}}^y @ \text{SL1} &= -J_{\text{NSC}}^y @ \text{SL2} \\ &= \sigma_{\text{NSC}}^{y,xx}(0, \omega, -\omega)(|E^x|^2 - |E^y|^2). \end{aligned} \quad (9)$$

The layer contributing opposite NSC can be understood by the fact that NSC is \mathcal{PT} odd, and the two MBT SLs can be mapped via $\mathcal{PT}\mathbf{x}_{\text{SL1}} = \mathbf{x}_{\text{SL2}}$ (\mathbf{x} includes both spatial coordinates and local magnetic moments). On the other hand, the MIC $\eta_{\text{MIC}}^{a,bb}(0, \omega, -\omega)$ is determined by velocity difference Δ_{nm}^a and quantum metric g_{nm}^{bb} between bands n and m . Under $\mathcal{M}_x\mathcal{T}$, one has $\Delta_{nm}^y(k_x, k_y) = -\Delta_{nm}^y(k_x, -k_y)$ and $g_{nm}^{bb}(k_x, k_y) = g_{nm}^{bb}(k_x, -k_y)$. In this regard, MIC flows along x and must vanish along y , namely, $\eta_{\text{MIC}}^{y,bb}(0, \omega, -\omega) = 0$. One

TABLE I. Transformation symmetries of different quantities (\mathbf{k} coordinate, shift vector, quantum metric, velocity difference, and spin operator) under spatial and time-reversal operators.

| | \mathcal{M}_i | \mathcal{P} | \mathcal{T} | $\mathcal{M}_i\mathcal{T}$ | \mathcal{PT} |
|-----------------|--|------------------|------------------|--|-----------------|
| (k_x, k_y) | $(-k_x, k_y)$ | $(-k_x, -k_y)$ | $(-k_x, -k_y)$ | $(k_x, -k_y)$ | (k_x, k_y) |
| $R_{nm}^{a,b}$ | $(-1)^{\delta_{ia}} R_{nm}^{a,b}$ | $-R_{nm}^{a,b}$ | $R_{nm}^{a,b}$ | $(-1)^{\delta_{ia}} R_{nm}^{a,b}$ | $-R_{nm}^{a,b}$ |
| g_{nm}^{bc} | $(-1)^{\delta_{ib}+\delta_{ic}} g_{nm}^{bc}$ | g_{nm}^{bc} | g_{nm}^{bc} | $(-1)^{\delta_{ib}+\delta_{ic}} g_{nm}^{bc}$ | g_{nm}^{bc} |
| Δ_{nm}^a | $(-1)^{\delta_{ia}} \Delta_{nm}^a$ | $-\Delta_{nm}^a$ | $-\Delta_{nm}^a$ | $(-1)^{\delta_{ia}+1} \Delta_{nm}^a$ | Δ_{nm}^a |
| S_{nm}^d | $(-1)^{\delta_{id}+1} S_{nm}^d$ | S_{nm}^d | $-S_{nm}^d$ | $(-1)^{\delta_{id}} S_{nm}^d$ | $-S_{nm}^d$ |

then has

$$\begin{aligned} \frac{dj_{\text{MIC}}^x}{dt} @\text{SL1} &= \frac{dj_{\text{MIC}}^x}{dt} @\text{SL2} \\ &= \eta_{\text{MIC}}^{x,xx}(0, \omega, -\omega)(|E^x|^2 - |E^y|^2). \end{aligned} \quad (10)$$

The MIC generation is \mathcal{PT} even; hence, the two SLs give the same results. These discussions are consistent with magnetic group theory results [25]. Therefore, we suggest that the layer-dependent photocurrent directions of NSC and MIC under x -LPL would be vertical, so that their detection and measurement can be performed individually. We tabulate the spatial and time-reversal transformation of various gauge-invariant quantities in Table I.

To verify these symmetry analyses, we plot our first-principles calculation results in Figs. 1(c)–1(e). Consistent with our argument, the $\sigma_{\text{NSC}}^{x,xx}(0, \omega, -\omega)$ is always zero, which is not shown for clarity. The $\sigma_{\text{NSC}}^{y,xx}(0, \omega, -\omega)$ on the SL1 reaches $-90.9 \mu\text{A}/\text{V}^2$ at an incident photon energy $\omega = 0.69 \text{ eV}$ [Fig. 1(c)]. Note that this value surpasses the NSC photoconductivity calculated in many other two-dimensional (2D) materials, such as MoS_2 [61], GeS [60], and $\alpha\text{-NP}$ [62]. Hence, an x -LPL at this photon energy with alternating electric field magnitude $E = 0.5 \text{ V/nm}$ could trigger a current density of $-22.7 \mu\text{A}/\text{nm}^2$, with the negative sign indicating current along $-y$. To clearly show the BZ contribution, we depict the shift vector $R_{vc}^{x,xx}(\mathbf{k})@SL1$, where clear symmetries between (k_x, k_y) and $(k_x, -k_y)$ can be observed [Fig. 1(d)], confirming its transformation as a polar vector. The NSC

integrand $\zeta^{y,xx}(\mathbf{k}, \omega)$ is plotted [Fig. 1(e)], which suggests that the NSC is mainly contributed from the vicinity of the Γ point. The other SL contributes oppositely to the NSC (with an opposite shift vector). As a result, the net NSC of the MBT-MBT bilayer is zero, which has been largely overlooked previously. Nevertheless, in this paper, we propose that there emerges a hidden layer-dependent NSC with a large magnitude. The vdW gap that separates the two SLs allows one to detect such a NSC with well-deposited electrodes.

As for the MIC generation, $\eta_{\text{MIC}}^{x,xx}(0, \omega, -\omega)$ on both SLs contributed equally [Fig. 2(a)], while the calculated $\eta_{\text{MIC}}^{y,xx}(0, \omega, -\omega)$ is always zero. The calculated $\eta_{\text{MIC}}^{x,xx}(0, \omega, -\omega)$ is consistent with previous works, further verifying our numerical procedure. Each SL yields a MIC of $-60.0 \times 10^8 \text{ A}/(\text{V}^2 \text{ s})$ (at an incident photon energy of $\omega = 0.61 \text{ eV}$). One could then expect a current density of $-300.0 \mu\text{A}/\text{nm}^2$ under x -LPL with $E = 0.5 \text{ V/nm}$ (at the same photon energy), assuming an effective electron lifetime of 0.2 ps . Note that this value is conservative and could be even longer, depending on the sample quality and environmental condition. The \mathbf{k} -resolved velocity difference between the top valence and bottom conduction bands are plotted [Fig. 2(b)]. The symmetry argument of $\Delta_{vc}^x(k_x, k_y) = \Delta_{vc}^x(k_x, -k_y)$ is clearly observed. Note that the two SLs possess the same $\Delta_{vc}^x(\mathbf{k})$. The quantum metric shows a similar pattern [Fig. 2(c)]. The integrand of MIC, $\zeta(\mathbf{k}, \omega)@SL1$, is plotted for $\omega = 0.61 \text{ eV}$, where large contributions in the vicinity of Γ are seen [Fig. 2(d)].

In addition to charge current that uses electric charge as the degree of freedom to carry information, electronic spin can serve as another information carrier, which is facile to tune and easy to detect as well. In some recent works, photon illumination generated spin current has been predicted and evaluated in various material platforms [60,61]. Here, we extend the LPL-induced charge photocurrent into spin photocurrent that remains for further discussion or evaluation in \mathcal{PT} systems [63]. We adopt the anticommutation definition of the spin-current operator that has been widely used during the past decade. One must note that the spin-torque effect may arise when the spin operator is not a good quantum number under SOC [54,64]. This could be small in magnetic materials for intrinsic spin polarization. Under LPL, the spin current also comprises MIC and NSC nature, which

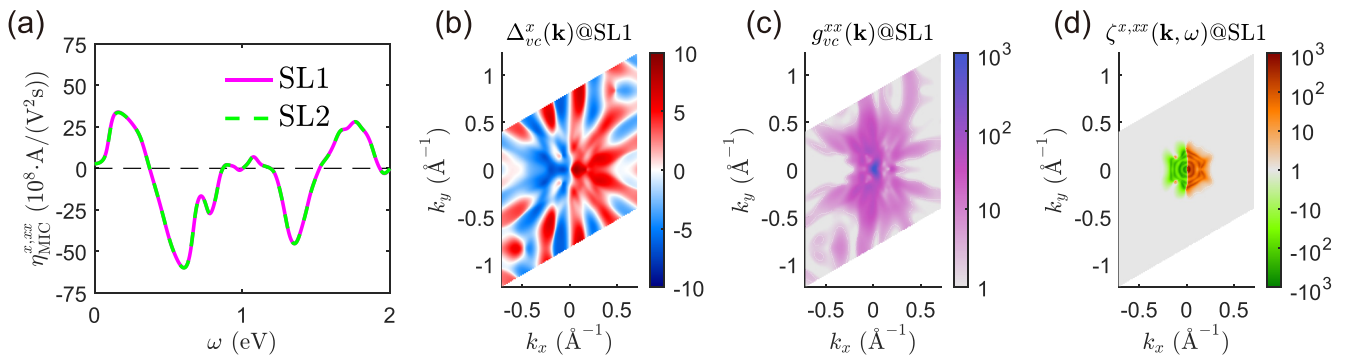


FIG. 2. Magnetic injection current (MIC) in the MBT-MBT bilayer. (a) The calculated MIC on MBT septuple layers (SLs) under x -linearly polarized light (LPL). Only the x -flowing current is finite, while the y current is forbidden. (b) Velocity difference $\Delta_{vc}^x(\mathbf{k})@SL1$ and (c) quantum metric distribution $g_{vc}^{xx}(\mathbf{k})@SL1$ over the first Brillouin zone (BZ). (d) \mathbf{k} -resolved MIC integrand $\zeta(\mathbf{k}, \omega)@SL1$ at $\omega = 0.61 \text{ eV}$. In these plots, the symmetries of (k_x, k_y) and $(k_x, -k_y)$ are clearly seen.

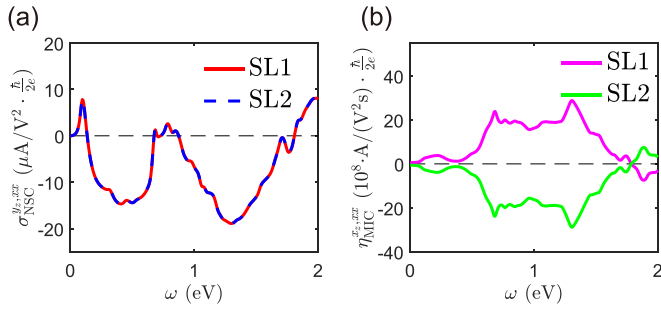


FIG. 3. Spin photocurrents in the MBT-MBT bilayer. (a) The spin normal shift current (NSC) photoconductance in the two septuple layers (SLs) under x -linearly polarized light (LPL). (b) The spin magnetic injection current (MIC) photoconductance in the two SLs under x -LPL. The spin NSC flowing along x ($\sigma_{NSC}^{x_z,xx}$) and spin MIC flowing along y ($\eta_{MIC}^{y_z,xx}$) are both symmetrically forbidden.

are depicted in Fig. 3. One sees that the spin NSCs are the same for both SLs and flow along y , $\sigma_{NSC}^{y_z,xx}(0, \omega, -\omega)$ @SL1 = $\sigma_{NSC}^{y_z,xx}(0, \omega, -\omega)$ @SL2 $\neq 0$, while $\sigma_{NSC}^{x_z,xx}(0, \omega, -\omega) = 0$ under $\mathcal{M}_x\mathcal{T}$ symmetry constraints. This is because spin operator \hat{S}_z is symmetrically unchanged under $\mathcal{M}_x\mathcal{T}$. Similarly, the spin MICs are opposite in the two SLs, which flow along x , namely, $\eta_{MIC}^{x_z,xx}(0, \omega, -\omega)$ @SL1 = $-\eta_{MIC}^{x_z,xx}(0, \omega, -\omega)$ @SL2 $\neq 0$, yielding zero net spin MIC in the whole system. Therefore, like charge current, the spin NSC and MIC also flow vertically to each other. When one sums the two SLs together, the charge MIC survives which transports along x , while the spin NSC is nonzero, flowing along y . This causes pure spin current to arise, which carries no charge carriers and plays an essential

role for the low-energy cost and high-efficiency spintronics [65,66].

We next show that magnetic configuration could tune these photocurrents. If the time-reversal AFM configuration is used, the charge NSC remains their values since they are \mathcal{T} even. At the same time, the charge MIC reverses its direction, being a \mathcal{T} -odd quantity. However, for the spin current, since S_z adds another \mathcal{T} -odd operator, the spin NSC remains its value while spin MIC becomes the opposite. We plot our calculations in Fig. S2 in the Supplemental Material [15]. The FM interlayer configuration, which has been successfully achieved in recent experiments, is equivalent to posing time-reversal \mathcal{T} onto one of these two SLs (see the band dispersion in Fig. S3 in the Supplemental Material [15]). It reverses the charge MIC (and spin NSC) in such a SL while keeping charge NSC (and spin MIC). Note that the exact photoconductivity values are slightly changed because the band structure is altered (Fig. S4 in the Supplemental Material [15]). In this regard, all the charge and spin currents become opposite in the two SLs, giving zero net (charge and spin) NSC and MIC. This is consistent with the fact that the FM MBT-MBT bilayer is \mathcal{P} symmetric. These results are also plotted in Fig. S5 in the Supplemental Material [15]. Therefore, we propose that one could apply a magnetic field to toggle and achieve various layer-resolved charge and spin photocurrents.

B. Photocurrents of MBT-BT-MBT trilayer ($Mn_2Bi_6Te_{11}$)

We then intercalate a BT QL inside the MBT-MBT bilayers, forming a MBT-BT-MBT trilayer [Fig. 4(a)]. The two MBT SLs prefer a weak AFM configuration, which is

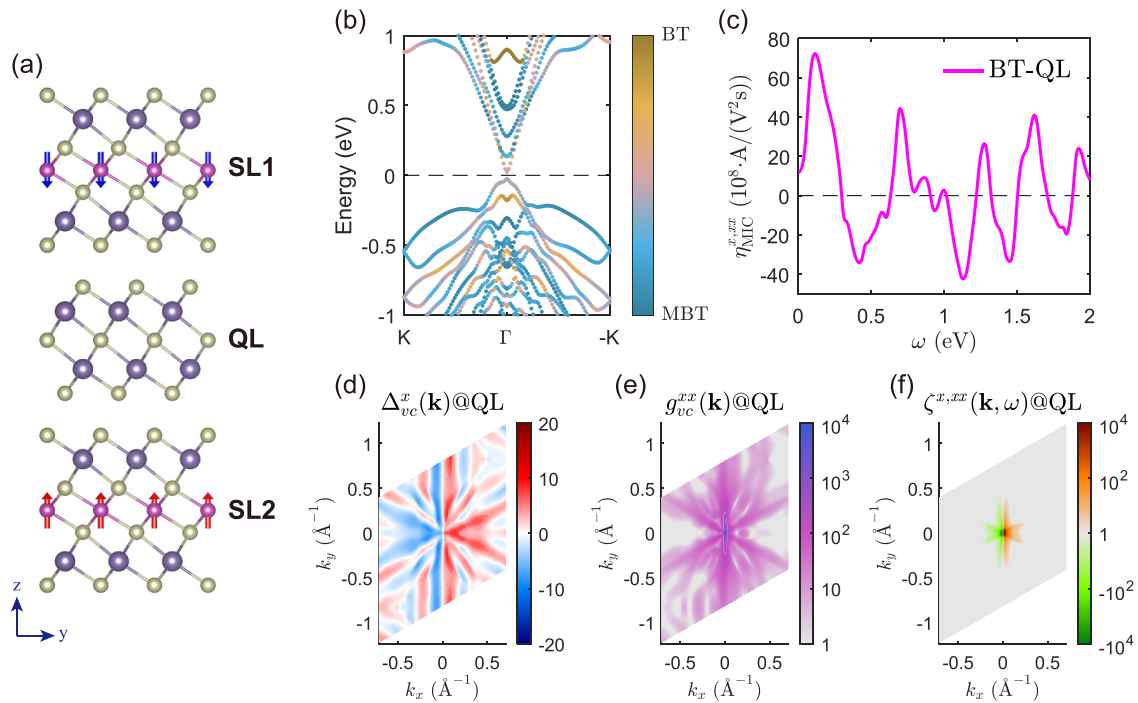


FIG. 4. Photocurrents in MBT-BT-MBT trilayer under x -linearly polarized light (LPL). (a) Geometric structure of MBT-BT-MBT trilayer, with arrows indicating local magnetic moments on the Mn atoms. (b) Band dispersion along the high-symmetric \mathbf{k} -path with contributions from the BT quintuple layer (QL) highlighted. (c) The magnetic injection current (MIC) photoconductivity of the central BT QL. Brillouin zone distribution of (d) $\Delta_{vc}^x(\mathbf{k})$ @QL and (e) $g_{vc}^{xx}(\mathbf{k})$ @QL between the valence and conduction bands. (f) \mathbf{k} -resolved $\zeta^{x,xx}(\mathbf{k}, \omega)$ @QL at $\omega = 0.11$ eV.

energetically lower than the interlayer FM state by 0.12 meV per unit cell. The significantly reduced magnetic exchange energy is ascribed by the long-range coupling between the two MBT SLs. The band dispersion is plotted in Fig. 4(b), where contributions from the BT QL are highlighted by the color map. The direct bandgap becomes 51 meV and shows no spin-polarization feature owing to the \mathcal{PT} symmetry in the whole system. We verify that the local magnetic moments on the BT QL vanish, under the magnetic proximity of two AFM aligned MBT SLs.

We plot the calculated charge NSC $\sigma_{\text{NSC}}^{y,xx}(0, \omega, -\omega)$ and MIC $\eta_{\text{MIC}}^{x,xx}(0, \omega, -\omega)$ on the two MBT SLs in Fig. S6 in the Supplemental Material [15]. Like in the MBT-MBT bilayer case, the former is opposite in the two MBT SLs, while the latter shows the same value (and magnitude) on both SLs. Both lie on the same order of magnitude as those in the MBT-MBT bilayer system. Interestingly, we find that the central BT QL exhibits a large MIC type photocurrent [Fig. 4(c)], even though the BT QL is spatially centrosymmetric and shows no local magnetizations on the Bi and Te atoms. The magnetic proximity effect from MBT SLs break the spatial symmetry magnetically (magnetic point group of $\bar{3}'m'$) via vdW interfacial coupling. One has to note that, unlike intrinsically magnetic systems (such as MBT-MBT bilayer [11], AFM CrI₃-CrI₃ bilayer, and bulk α -Fe₂O₃ [63]), here, the BT QL does not show finite local magnetic moments. The calculated MIC reaches 72.4×10^8 A/(V² s) (at incident energy $\omega = 0.11$ eV) and flows along x , which is much larger than the calculated values in the CrI₃ bilayer. Thus, a light with 3.3×10^{10} W/cm² could inject a current density of $361.8 \mu\text{A}/\text{nm}^2$ (assuming carrier lifetime of 0.2 ps). We plot the $\Delta_{vc}^x(\mathbf{k})@QL$ and $g_{vc}^{xx}(\mathbf{k})@QL$ distributions in Figs. 4(d) and 4(e), which yield large contributions around the Γ point. The mirror symmetry is clearly observed. Together with joint density of states, one obtains the $\zeta(\mathbf{k}, \omega)@QL$ texture [Fig. 4(f)]. Since the intercalated BT QL is \mathcal{PT} symmetric, the NSC would vanish. This is also consistent with our numerical calculations.

To further demonstrate the interfacial magnetic proximity effect, we artificially move the two MBT SLs away from the BT QL and calculate photocurrents. The results are plotted in Fig. S7 in the Supplemental Material [15]. It shows that, as the interlayer distance gradually increases from 2.9 Å (equilibrium) to 6 Å, the magnitude of MIC reduces but with evident values. When the MBT is sufficiently apart from BT QL, the MIC vanishes. It clearly suggests that the interfacial magnetic proximity is the key mechanism to break \mathcal{P} in this situation, unlike previously reported routes.

We also plot the spin photocurrent of BT QL under x -LPL. According to the symmetric argument, it has spin NSC nature and flows along y . Other spin BPV photocurrents are symmetrically forbidden. The results are shown in Fig. 5. The perpendicular flow direction of charge and spin current indicates a pure spin current nature, like in other 2D nonmagnetic systems (such as MoS₂ [61] and GeS [60]). We see that, at $\omega = 1.36$ eV, $\sigma_{\text{NSC}}^{y,xx}(0, \omega, -\omega)@QL$ reaches $-59.7 \mu\text{A}/\text{V}^2(\hbar/2e)$, surpassing the calculated values in the CrI₃ bilayer [63] and BaFeO₃ [67]. The distribution of $\zeta(\mathbf{k}, \omega)@QL$ shows clear mirror symmetry.

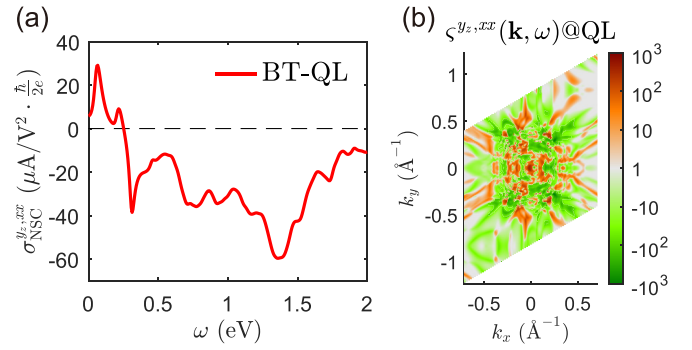


FIG. 5. Spin photocurrents on the BT quintuple layer (QL) in the MBT-BT-MBT trilayer under x -linearly polarized light (LPL). (a) Spin normal shift current (NSC) of BT $\sigma_{\text{NSC}}^{y,xx}(0, \omega, -\omega)@QL$. (b) k -resolved $\zeta(\mathbf{k}, \omega)@QL$ at $\omega = 1.36$ eV.

The magnetic order of MBT SLs also tunes the layer-specific photocurrents. The time reversal of AFM could reverse the charge MIC and spin NSC at BT QL (Fig. S8 in the Supplemental Material [15]), as \mathcal{T} flips the sign of Δ_{nm}^x and S_{nm}^z , respectively. Recent experiments show that the MBT SLs can transit into FM alignment under a much weaker magnetic field (0.22 T at 2 K) [26], owing to the long-range coupling between them. In the FM state, the symmetry of MBT-BT-MBT becomes \mathcal{P} ; then only charge and spin photocurrents appear on the MBT SLs, while the BT is completely silent (Fig. S9 in the Supplemental Material [15]) even though it is slightly magnetized.

C. Photocurrents of MBT-BT-BT-MBT tetralayer (Mn₂Bi₅Te₁₄)

Finally, we propose that such an approach can be extended into thicker superlattice thin films, such as a MBT-BT-BT-MBT tetralayer [Fig. 6(a)]. We plot the charge and spin photocurrents on the MBT SLs in Fig. S10 in the Supplemental Material [15] and those localized on the two BT QLs (QL1 and QL2) in Figs. 6(b)–6(e). Similarly, the charge NSC along x and MIC along y are symmetrically forbidden. We see that $\sigma_{\text{NSC}}^{y,xx}(0, \omega, -\omega)@QL1 = -\sigma_{\text{NSC}}^{y,xx}(0, \omega, -\omega)@QL2 \neq 0$ and $\eta_{\text{MIC}}^{x,xx}(0, \omega, -\omega)@QL1 = \eta_{\text{MIC}}^{x,xx}(0, \omega, -\omega)@QL2 \neq 0$. The magnitude of these photocurrents is large enough to be observed experimentally, suggesting the capacity of \mathcal{P} broken under the magnetic proximity effect. As for the spin-current generation, the spin NSC satisfies $\sigma_{\text{NSC}}^{y,xx}(0, \omega, -\omega)@QL1 = \sigma_{\text{NSC}}^{y,xx}(0, \omega, -\omega)@QL2 \neq 0$ (the x -direction spin NSC is forbidden), and spin MIC is $\eta_{\text{MIC}}^{x,xx}(0, \omega, -\omega)@QL1 = -\eta_{\text{MIC}}^{x,xx}(0, \omega, -\omega)@QL2 \neq 0$ (the y -direction spin MIC is forbidden), which generally is normal to the charge current. If one adds the QL1 and QL2 responses together, it is qualitatively the same as that of BT QL in the MBT-BT-MBT system. Note that different magnetic configurations in the MBT SLs could also control the charge and spin photocurrents localized on specific vdW layers (Fig. S11 in the Supplemental Material [15]).

IV. DISCUSSION

We schematically depict the mechanism and propose the potential measurement setup in Fig. 7. As demonstrated

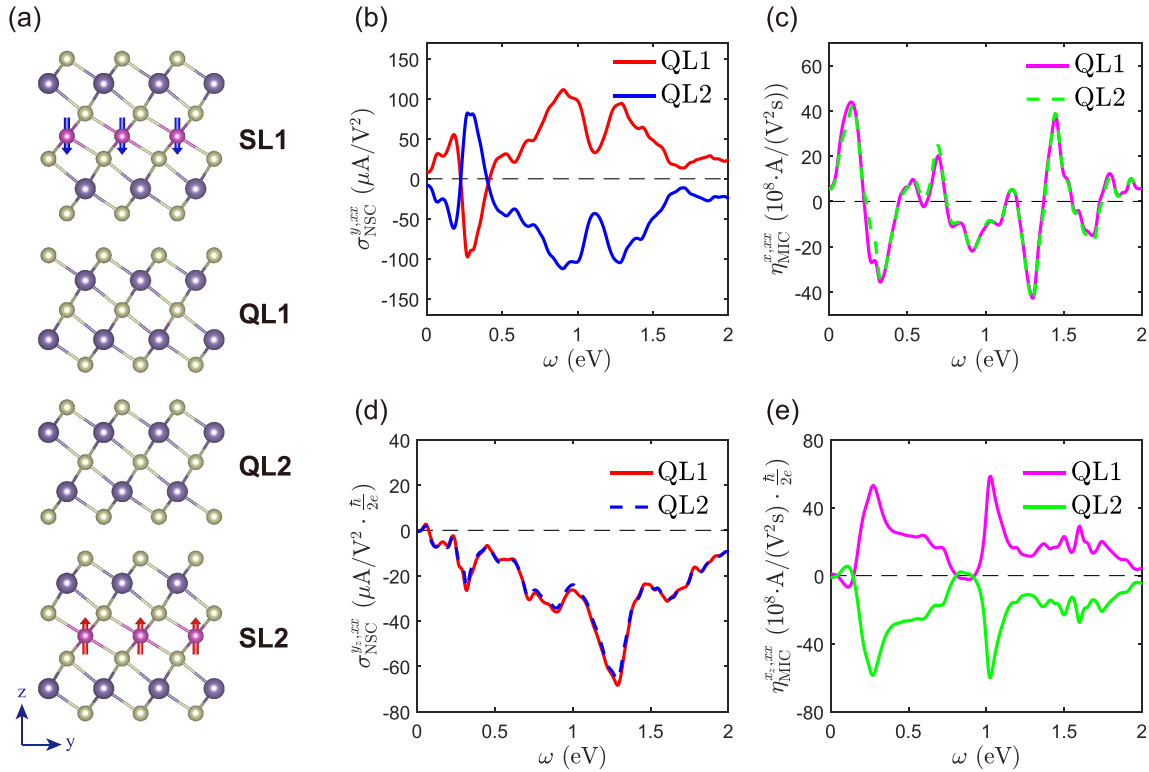


FIG. 6. Charge and spin photocurrents on quintuple layers (QLs) in the MBT-BT-BT-MBT tetralayer under x -linearly polarized light (LPL). (a) Atomic geometric structure and magnetic alignment of the MBT-BT-BT-MBT tetralayer. (b) Charge normal shift current (NSC) of the two BT QLs, $\sigma_{\text{NSC}}^{y,xx}(0, \omega, -\omega)$ @QL1 and $\sigma_{\text{NSC}}^{y,xx}(0, \omega, -\omega)$ @QL2, showing opposite flowing directions with same magnitude. (c) Charge magnetic injection current (MIC) $\eta_{\text{MIC}}^{x,xx}(0, \omega, -\omega)$ @QL1 and $\eta_{\text{MIC}}^{x,xx}(0, \omega, -\omega)$ @QL2, which are the same in both magnitude and direction. (d) Spin NSC $\sigma_{\text{NSC}}^{z,xx}(0, \omega, -\omega)$ and (e) spin MIC $\eta_{\text{MIC}}^{z,xx}(0, \omega, -\omega)$ localized on the two BT QLs.

previously, the charge and spin currents flow vertically [Fig. 7(a)], which become silent after removing the AFM sandwich layers or when they form FM configuration. One notes that the AFM configuration can be fine-tuned via an

external magnetic field, forming a double hysteresis loop on reversing the field sweep [Fig. 7(b)]. Accordingly, the charge and spin BPV currents would emerge and diminish with respect to proximate magnetic orders [Fig. 7(c)].

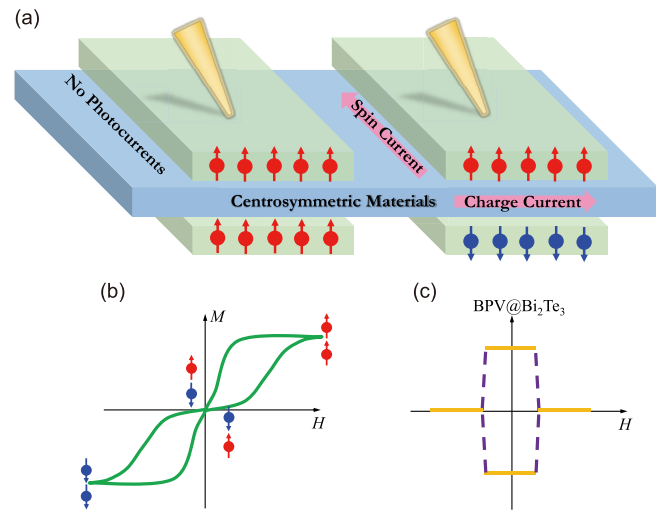


FIG. 7. Schematic plot of bulk photovoltaic (BPV) currents measurement. (a) Antiferromagnetic (AFM) sandwich could generate BPV currents in spatially centrosymmetric layers, which is silent intrinsically. (b) Magnetic hysteresis loop of AFM system, and (c) plots the magnetic field controlled BPV photoconductivity.

In this paper, we illustrate a potential approach to detect hidden physical responses such as hidden spin polarization and hidden layer photocurrent generation. The antiunitary constrained double degeneracy in each band hinders direct measurement on the hidden spin polarization that arises from the local symmetry broken in specific sectors (or vdW layers). Here, we suggest that this hidden spin polarization may be indirectly determined from the emergence of spin MIC since both spin polarization and the spin quantum metric are opposite in the two SLs, giving sizable multiplication. This is also like the hidden layer Hall effect that has been recently discovered [68] and may be referred to as the hidden layer photocurrent effect. One potential measurement is to apply gate voltage and trace the emergence and reversal of the BPV current under positive and negative gate field [11].

The photoconductivity that arises from the magnetic SL also provides a facile way to detect and measure the axion insulating phase that usually appears in AFM layered materials. In axion insulators, the top and bottom layers that contribute $\frac{1}{2}$ and $-\frac{1}{2}$ Chern numbers can be connected via a \mathcal{PT} operator. The total Chern number is zero in an intrinsic axion insulator, which would provide a nonzero Chern number when \mathcal{T} is broken under an external magnetic field. Here, we show that

TABLE II. LPL induced photocurrents under different symmetry operators. The mirror normal direction i and j are x or y , so that the spin polarization S_z always flips its sign under a mirror operator.

| | σ_{NSC}^j | η_{MIC}^j | σ_{NSC}^{jz} | η_{MIC}^{jz} |
|----------------------------|-------------------------|-----------------------|----------------------------|--------------------------|
| $\mathcal{M}_i (i \neq j)$ | Even | Even | Odd | Odd |
| \mathcal{M}_j | Odd | Odd | Even | Even |
| \mathcal{P} | Odd | Odd | Odd | Odd |
| \mathcal{T} | Even | Odd | Odd | Even |

the charge MIC is even under \mathcal{PT} . Hence, the total MIC is nonzero in an intrinsic axion insulator. This would provide an additional route for measuring axion insulators and does not require a magnetic field.

In our evaluations, we only focused on the x -polarized LPL. Since the system is C_{3z} rotational invariant, the y -polarized LPL irradiation would induce similar (charge and spin) BPV photocurrents with a sign change. Hence, the carrier motion can be effectively manipulated by the polarization direction of LPL (obeying a sinusoidal function with respect to polarization angle). As for the CPL, it would introduce additional photocurrent via its phase factor. Generally, such a phase factor results in 90° -rotated photocurrents. The shift and injection nature swaps as well.

We summarize the mirror reflection, spatial central inversion, and time-reversal impacts on the LPL-induced charge and spin photocurrents in Table II. Even and odd indicate whether, under a specific operation, such a BPV current would keep or flip its sign, respectively. Their combination can be easily deduced. For example, the \mathcal{PT} symmetry assigns odd charge NSC and even charge MIC, so that the former is vanished and the latter can be finite. Here, we provide mirror reflection results, which can be viewed as a directional spatial inversion, aiding detailed discussion of different photocurrent components. In addition, the layer-dependent BPV current can be analyzed here. For example, in the AFM MBT-BT-MBT trilayer, the two MBT SLs are connected by \mathcal{PT} ($\mathcal{PT}\mathbf{x}_{\text{SL1}} = \mathbf{x}_{\text{SL2}}$). Thus, the charge NSC and spin MIC in these SLs flow oppositely, while the charge MIC and spin NSC will be the same. Each MBT SL is $\mathcal{M}_x\mathcal{T}$; thus, σ_{NSC}^x , η_{MIC}^y , σ_{NSC}^z , and η_{MIC}^z are all symmetrically forbidden.

One may wonder if out-of-plane BPV conductivity components of 2D materials can be similarly calculated and discussed. In the current theoretical framework, an in-plane electric field component corresponds to normal incidence of light. Then the periodicity in the xy plane eliminates the edge or end effects. According to previous work [69], this is akin to the closed-circuit boundary condition, where electric field \mathbf{E} can be used as the natural variable. As is well known, in a finite-sized system, the edge or end effect could accumulate induced charges and drastically change the boundary condition. The out-of-plane electric field component corresponds to tangential incidence, which is experimentally challenging for thin films. In addition, the boundary condition becomes an

open circuit feature, and the charge accumulation on the film surface could be significant. In this situation, one should, in principle, adopt electric displacement \mathbf{D} rather than \mathbf{E} as the natural variable. On the other hand, the response function, formulated via Kubo perturbation theory [3], evaluates (charge and spin) current density. This definition is also in-plane, while it would be ill defined for the out-of-plane current. Note that the z direction is quantum confined for thin films; hence, it is challenging to define a current along z . Recently, it was proposed that such an out-of-plane response is an electric dipole, which requires evaluations of Wannier centers [70]. Nonetheless, the functions in this paper cannot be straightforwardly applied for out-of-plane component calculations.

We would like to remark that the magnetic direction would change the symmetry arguments since spin is a pseudovector. In this paper, we only focus on the easy-axis magnetic direction (z), which preserves the C_{3z} rotation. If the magnetic moment is aligned in the xy plane or when paramagnetic configuration emerges, $\mathcal{M}_x\mathcal{T}$ symmetry breaks, so that the photocurrents would change their mechanisms and flowing direction due to the reduction of its magnetic group. This is out of the scope of this paper and will be discussed elsewhere.

V. CONCLUSIONS

In this paper, we systematically calculate the layer-dependent photocurrent responses of MBT and BT superlattice thin films. Various sources of charge and spin BPV effects have been evaluated, and we provide symmetry constraints and arguments in detail. We show that, even though a nonmagnetic BT QL is spatially centrosymmetric, one can break \mathcal{P} via applying the magnetic proximity effect through the vdW interfaces. In this regard, large charge and spin BPV currents can be generated. The directions of charge and spin current are vertical to each other, yielding pure charge and spin BPV photocurrent simultaneously. This strategy is different from previously proposed \mathcal{P} -broken methods in otherwise nonmagnetic systems, such as introducing dopants, manipulating structures, or applying electric bias. The BPV charge and spin currents can be tuned by magnetic configuration, light polarization, and interfacial effects. In addition to BPV generation, another second-order nonlinear optical response—second harmonic generation—may show such a MBT SL or BT QL layer-dependent feature, and our approach can be directly applied to the recently discovered surface second harmonic generation measurements [71] and provide a potential explanation.

ACKNOWLEDGMENTS

This paper was supported by the National Natural Science Foundation of China under Grants No. 11974270 and No. 21903063. The computational resources from the high-performance computing platform of Xi'an Jiaotong University and Hefei Advanced Computing Center are also acknowledged.

[1] V. M. Fridkin, Bulk photovoltaic effect in noncentrosymmetric crystals, *Crystallogr. Rep.* **46**, 654 (2001).

[2] A. M. Glass, D. von der Linde, and T. J. Negran, High-voltage bulk photovoltaic effect and the

- photorefractive process in LiNbO_3 , *Appl. Phys. Lett.* **25**, 233 (1974).
- [3] R. von Baltz and W. Kraut, Theory of the bulk photovoltaic effect in pure crystals, *Phys. Rev. B* **23**, 5590 (1981).
- [4] W. Shockley and H. J. Queisser, Detailed balance limit of efficiency of p - n junction solar cells, *J. Appl. Phys.* **32**, 510 (1961).
- [5] S. Kahmann and M. A. Loi, Hot carrier solar cells and the potential of perovskites for breaking the Shockley-Queisser limit, *J. Mater. Chem. C* **7**, 2471 (2019).
- [6] J. A. Armstrong, N. Bloembergen, J. Ducuing, and P. S. Pershan, Interactions between light waves in a nonlinear dielectric, *Phys. Rev.* **127**, 1918 (1962).
- [7] N. Bloembergen and P. S. Pershan, Light waves at the boundary of nonlinear media, *Phys. Rev.* **128**, 606 (1962).
- [8] J. E. Sipe and A. I. Shkrebtii, Second-order optical response in semiconductors, *Phys. Rev. B* **61**, 5337 (2000).
- [9] S. M. Young and A. M. Rappe, First Principles Calculation of the Shift Current Photovoltaic Effect in Ferroelectrics, *Phys. Rev. Lett.* **109**, 116601 (2012).
- [10] F. Nastos and J. E. Sipe, Optical rectification and current injection in unbiased semiconductors, *Phys. Rev. B* **82**, 235204 (2010).
- [11] H. Wang and X. Qian, Electrically and magnetically switchable nonlinear photocurrent in PT -symmetric magnetic topological quantum materials, *npj Comput. Mater.* **6**, 199 (2020).
- [12] Y. Zhang, T. Holder, H. Ishizuka, F. de Juan, N. Nagaosa, C. Felser, and B. Yan, Switchable magnetic bulk photovoltaic effect in the two-dimensional magnet CrI_3 , *Nat. Commun.* **10**, 3783 (2019).
- [13] R. Fei, W. Song, and L. Yang, Giant photogalvanic effect and second-harmonic generation in magnetic axion insulators, *Phys. Rev. B* **102**, 035440 (2020).
- [14] H. Chen, M. Ye, N. Zou, B.-L. Gu, Y. Xu, and W. Duan, Basic formulation and first-principles implementation of nonlinear magneto-optical effects, *Phys. Rev. B* **105**, 075123 (2022).
- [15] See Supplemental Material at <http://link.aps.org/supplemental/10.1103/PhysRevResearch.5.013001> for the detailed symmetry analysis by group theory and band structures of all systems without SOC. In addition, supplemental figures are plotted for photocurrents affected by the time reversal effect, tuned magnetic configurations, and vdW layer distance.
- [16] H. Xu, H. Wang, J. Zhou, Y. Guo, J. Kong, and J. Li, Colossal switchable photocurrents in topological Janus transition metal dichalcogenides, *npj Comput. Mater.* **7**, 31 (2021).
- [17] J. Jiang, Z. Chen, Y. Hu, Y. Xiang, L. Zhang, Y. Wang, G. C. Wang, and J. Shi, Flexo-photovoltaic effect in MoS_2 , *Nat. Nanotechnol.* **16**, 894 (2021).
- [18] H. Xu, H. Wang, and J. Li, Nonlinear nonreciprocal photocurrents under phonon dressing, *Phys. Rev. B* **106**, 035102 (2022).
- [19] Y. Shi and J. Zhou, Coherence control of directional nonlinear photocurrent in spatially symmetric systems, *Phys. Rev. B* **104**, 155146 (2021).
- [20] A. M. Schankler, L. Gao, and A. M. Rappe, Large bulk piezophotovoltaic effect of monolayer $2H$ - MoS_2 , *J. Chem. Phys.* **12**, 1244 (2021).
- [21] H. Li, X. Yu, X. Shen, G. Tang, and K. Han, External electric field induced second-order nonlinear optical effects in hexagonal graphene quantum dots, *J. Phys. Chem. C* **123**, 20020 (2019).
- [22] L. Du, T. Hasan, A. Castellanos-Gomez, G.-B. Liu, Y. Yao, C. N. Lau, and Z. Sun, Engineering symmetry breaking in 2D layered materials, *Nat. Rev. Phys.* **3**, 193 (2021).
- [23] M. Bora and P. Deb, Magnetic proximity effect in two-dimensional van der Waals heterostructure, *J. Phys. Mater.* **4**, 034014 (2021).
- [24] A. K. Geim and I. V. Grigorieva, Van der Waals heterostructures, *Nature (London)* **499**, 419 (2013).
- [25] T. Bjorkman, A. Gulans, A. V. Krasheninnikov, and R. M. Nieminen, van der Waals Bonding in Layered Compounds from Advanced Density-Functional First-Principles Calculations, *Phys. Rev. Lett.* **108**, 235502 (2012).
- [26] C. Hu, K. N. Gordon, P. Liu, J. Liu, X. Zhou, P. Hao, D. Narayan, E. Emmanouilidou, H. Sun, Y. Liu *et al.*, A van der Waals antiferromagnetic topological insulator with weak inter-layer magnetic coupling, *Nat. Commun.* **11**, 97 (2020).
- [27] H. Sun, B. Xia, Z. Chen, Y. Zhang, P. Liu, Q. Yao, H. Tang, Y. Zhao, H. Xu, and Q. Liu, Rational Design Principles of the Quantum Anomalous Hall Effect in Superlattice-like Magnetic Topological Insulators, *Phys. Rev. Lett.* **123**, 096401 (2019).
- [28] M. M. Otrokov, T. V. Menshchikova, M. G. Vergniory, I. P. Rusinov, A. Yu. Vyazovskaya, Yu. M. Koroteev, G. Bihlmayer, A. Ernst, P. M. Echenique, A. Arnau *et al.*, Highly-ordered wide bandgap materials for quantized anomalous Hall and magnetoelectric effects, *2D Mater.* **4**, 025082 (2017).
- [29] Y. Zhao and Q. Liu, Routes to realize the axion-insulator phase in $\text{MnBi}_2\text{Te}_4(\text{Bi}_2\text{Te}_3)_n$ family, *Appl. Phys. Lett.* **119**, 060502 (2021).
- [30] H. Tan and B. Yan, Facet dependent surface energy gap on magnetic topological insulators, *Phys. Rev. B* **105**, 165130 (2022).
- [31] J. Li, Y. Li, S. Du, Z. Wang, B.-L. Gu, S.-C. Zhang, K. He, W. Duan, and Y. Xu, Intrinsic magnetic topological insulators in van der Waals layered MnBi_2Te_4 -family materials, *Sci. Adv.* **5**, eaaw5685 (2019).
- [32] N. Mounet, M. Gibertini, P. Schwaller, D. Campi, A. Merkys, A. Marrazzo, T. Sohier, I. Eligio Castelli, A. Cepellotti, G. Pizzi *et al.*, Two-dimensional materials from high-throughput computational exfoliation of experimentally known compounds, *Nat. Nanotechnol.* **13**, 246 (2018).
- [33] J. Liu, Q. Sun, Y. Kawazoe, and P. Jena, Exfoliating biocompatible ferromagnetic Cr-trihalide monolayers, *Phys. Chem. Chem. Phys.* **18**, 8777 (2016).
- [34] A. M. Shikin, D. A. Estyunin, D. A. Glazkova, S. O. Fil'nov, and I. I. Klimovskikh, Electronic and spin structures of intrinsic antiferromagnetic topological insulators of the $\text{MnBi}_2\text{Te}_4(\text{Bi}_2\text{Te}_3)_m$ family and their magnetic properties (brief review), *JETP Lett.* **115**, 213 (2022).
- [35] G. Kresse and J. Furthmüller, Efficient iterative schemes for *ab initio* total-energy calculations using a plane-wave basis set, *Phys. Rev. B* **54**, 11169 (1996).
- [36] G. Kresse and J. Furthmüller, Efficiency of *ab-initio* total energy calculations for metals and semiconductors using a plane-wave basis set, *Comput. Mater. Sci.* **6**, 15 (1996).
- [37] P. E. Blöchl, Projector augmented-wave method, *Phys. Rev. B* **50**, 17953 (1994).
- [38] J. P. Perdew, K. Burke, and M. Ernzerhof, Generalized Gradient Approximation Made Simple, *Phys. Rev. Lett.* **77**, 3865 (1996).
- [39] H. J. Monkhorst and J. D. Pack, Special points for Brillouin-zone integrations, *Phys. Rev. B* **13**, 5188 (1976).

- [40] V. I. Anisimov, J. Zaanen, and O. K. Andersen, Band theory and Mott insulators: Hubbard U instead of Stoner I , *Phys. Rev. B* **44**, 943 (1991).
- [41] S. L. Dudarev, G. A. Botton, S. Y. Savrasov, C. J. Humphreys, and A. P. Sutton, Electron-energy-loss spectra and the structural stability of nickel oxide: an LSDA + U study, *Phys. Rev. B* **57**, 1505 (1998).
- [42] M. M. Otrokov, I. I. Klimovskikh, H. Bentmann, D. Estyunin, A. Zeugner, Z. S. Aliev, S. Gaß, A. U. B. Wolter, A. V. Koroleva, A. M. Shikin *et al.*, Prediction and observation of an antiferromagnetic topological insulator, *Nature (London)* **576**, 416 (2019).
- [43] I. I. Klimovskikh, M. M. Otrokov, D. Estyunin, S. V. Ereemeev, S. O. Filnov, A. Koroleva, E. Shevchenko, V. Voroshnin, A. G. Rybkin, I. P. Rusinov *et al.*, Tunable 3D/2D magnetism in the $(\text{MnBi}_2\text{Te}_4)(\text{Bi}_2\text{Te}_3)_m$ topological insulators family, *npj Quantum Mater.* **5**, 54 (2020).
- [44] S. Qi, R. Gao, M. Chang, Y. Han, and Z. Qiao, Pursuing the high-temperature quantum anomalous Hall effect in $\text{MnBi}_2\text{Te}_4/\text{Sb}_2\text{Te}_3$ heterostructures, *Phys. Rev. B* **101**, 014423 (2020).
- [45] S. Grimme, J. Antony, S. Ehrlich, and H. Krieg, A consistent and accurate ab initio parametrization of density functional dispersion correction (DFT-D) for the 94 elements H-Pu, *J. Chem. Phys.* **132**, 154104 (2010).
- [46] I. Souza, N. Marzari, and D. Vanderbilt, Maximally localized Wannier functions for entangled energy bands, *Phys. Rev. B* **65**, 035109 (2001).
- [47] N. Marzari and D. Vanderbilt, Maximally localized generalized Wannier functions for composite energy bands, *Phys. Rev. B* **56**, 12847 (1997).
- [48] G. Pizzi, V. Vitale, R. Arita, S. Blügel, F. Freimuth, G. Géranton, M. Gibertini, D. Gresch, C. Johnson, T. Koretsune *et al.*, WANNIER90 as a community code: new features and applications, *J. Phys. Condens. Matter* **32**, 165902 (2020).
- [49] D. H. Kobe, Gauge-invariant resolution of the controversy over length versus velocity forms of the interaction with electric dipole radiation, *Phys. Rev. A* **19**, 205 (1979).
- [50] J. E. Sipe and E. Ghahramani, Nonlinear optical response of semiconductors in the independent-particle approximation, *Phys. Rev. B* **48**, 11705 (1993).
- [51] J. Ahn, G.-Y. Guo, and N. Nagaosa, Low-Frequency Divergence and Quantum Geometry of the Bulk Photovoltaic Effect in Topological Semimetals, *Phys. Rev. X* **10**, 041041 (2020).
- [52] A. Taghizadeh, F. Hipolito, and T. G. Pedersen, Linear and nonlinear optical response of crystals using length and velocity gauges: effect of basis truncation, *Phys. Rev. B* **96**, 195413 (2017).
- [53] J.-M. Lihm and C.-H. Park, Comprehensive theory of second-order spin photocurrents, *Phys. Rev. B* **105**, 045201 (2022).
- [54] J. Shi, P. Zhang, D. Xiao, and Q. Niu, Proper Definition of Spin Current in Spin-Orbit Coupled Systems, *Phys. Rev. Lett.* **96**, 076604 (2006).
- [55] Y. Sun, X. Mu, Q. Xue, and J. Zhou, Tailoring photoinduced nonequilibrium magnetizations in In_2Se_3 bilayers, *Adv. Opt. Mater.* **10**, 2200428 (2022).
- [56] A. Laturia, M. L. Van de Put, and W. G. Vandenberghe, Dielectric properties of hexagonal boron nitride and transition metal dichalcogenides: from monolayer to bulk, *npj 2D Mater. Appl.* **2**, 6 (2018).
- [57] J. Zhou, H. Xu, Y. Li, R. Jaramillo, and J. Li, Opto-mechanics driven fast martensitic transition in two-dimensional materials, *Nano Lett.* **18**, 7794 (2018).
- [58] Y. Deng, Y. Yu, M. Z. Shi, Z. Guo, Z. Xu, J. Wang, X. H. Chen, and Y. Zhang, Quantum anomalous Hall effect in intrinsic magnetic topological insulator MnBi_2Te_4 , *Science* **367**, 895 (2020).
- [59] M. M. Otrokov, I. P. Rusinov, M. Blanco-Rey, M. Hoffmann, A. Yu. Vyazovskaya, S. V. Ereemeev, A. Ernst, P. M. Echenique, A. Arnau, and E. V. Chulkov, Unique Thickness-Dependent Properties of the van der Waals Interlayer Antiferromagnet MnBi_2Te_4 Films, *Phys. Rev. Lett.* **122**, 107202 (2019).
- [60] X. Mu, Y. Pan, and J. Zhou, Pure bulk orbital and spin photocurrent in two-dimensional ferroelectric materials, *npj Comput. Mater.* **7**, 61 (2021).
- [61] H. Xu, H. Wang, J. Zhou, and J. Li, Pure spin photocurrent in non-centrosymmetric crystals: Bulk spin photovoltaic effect, *Nat. Commun.* **12**, 4330 (2021).
- [62] N. T. Kaner, Y. Wei, T. Ying, X. Xu, W. Li, A. Raza, X. Li, J. Yang, Y. Y. Jiang, and W. Q. Tian, Giant shift photovoltaic current in group V-V binary nanosheets, *Adv. Theory Simul.* **5**, 2100472 (2022).
- [63] R. Fei, W. Song, L. Pusey-Nazzaro, and L. Yang, PT -Symmetry-Enabled Spin Circular Photogalvanic Effect in Antiferromagnetic Insulators, *Phys. Rev. Lett.* **127**, 207402 (2021).
- [64] A. Manchon and S. Zhang, Theory of spin torque due to spin-orbit coupling, *Phys. Rev. B* **79**, 094422 (2009).
- [65] D. D. Awschalom and M. E. Flatté, Challenges for semiconductor spintronics, *Nat. Phys.* **3**, 153 (2007).
- [66] S. A. Wolf, D. D. Awschalom, R. A. Buhrman, J. M. Daughton, S. von Molnár, M. L. Roukes, A. Y. Chtchelkanova, and D. M. Treger, Spintronics: A spin-based electronics vision for the future, *Science* **294**, 1488 (2001).
- [67] S. M. Young, F. Zheng, and A. M. Rappe, Prediction of a Linear Spin Bulk Photovoltaic Effect in Antiferromagnets, *Phys. Rev. Lett.* **110**, 057201 (2013).
- [68] A. Gao, Y.-F. Liu, C. Hu, J.-X. Qiu, C. Tzschaschel, B. Ghosh, S.-C. Ho, D. Bérubé, R. Chen, H. Sun *et al.* Layer Hall effect in a 2D topological axion antiferromagnetic, *Nature (London)* **595**, 521 (2021).
- [69] M. Stengel, N. A. Spaldin, and D. Vanderbilt, Electric displacement as the fundamental variable in electronic-structure calculations, *Nat. Phys.* **5**, 304 (2009).
- [70] Y. Gao, Y. Zhang, and D. Xiao, Tunable Layer Circular Photogalvanic Effect in Twisted Bilayers, *Phys. Rev. Lett.* **124**, 077401 (2020).
- [71] J. Fonseca, G. M. Diederich, D. Ovchinnikov, J. Cai, C. Wang, J. Yan, D. Xiao, and X. Xu, Anomalous second harmonic generation from atomically thin MnBi_2Te_4 , *Nano Lett.* **22**, 10134 (2022).